

# Incorporating Clinical Guidelines through Adapting Multi-modal Large Language Model for Prostate Cancer PI-RADS Scoring

Tiantian Zhang<sup>1\*</sup>, Manxi Lin<sup>2\*</sup>, Hongda Guo<sup>3</sup>, Xiaofan Zhang<sup>4,5</sup>, Ka Fung Peter Chiu<sup>3</sup>, Aasa Feragen<sup>2</sup>, Qi Dou<sup>1\*\*</sup>

- <sup>1</sup> Department of Computer Science and Engineering, The Chinese University of Hong Kong, Sha Tin, Hong Kong  
{qidou@cuhk.edu.hk}
- <sup>2</sup> Department of Applied Mathematics and Computer Science, Technical University of Denmark, Kongens Lyngby, Denmark
- <sup>3</sup> Department of Surgery, The Chinese University of Hong Kong, Sha Tin, Hong Kong
- <sup>4</sup> Shanghai Jiao Tong University, Shanghai, China
- <sup>5</sup> Shanghai Artificial Intelligence Laboratory, Shanghai, China

**Abstract.** The Prostate Imaging Reporting and Data System (PI-RADS) is pivotal in the diagnosis of clinically significant prostate cancer through MRI imaging. Current deep learning-based PI-RADS scoring methods often lack the incorporation of essential PI-RADS clinical guidelines (PICG) utilized by radiologists, potentially compromising scoring accuracy. This paper introduces a novel approach that adapts a multi-modal large language model (MLLM) to incorporate PICG into PI-RADS scoring without additional annotations and network parameters. We present a two-stage fine-tuning process aimed at adapting MLLMs originally trained on natural images to the MRI data domain while effectively integrating the PICG. In the first stage, we develop a domain adapter layer specifically tailored for processing 3D MRI image inputs and design the MLLM instructions to differentiate MRI modalities effectively. In the second stage, we translate PICG into guiding instructions for the model to generate PICG-guided image features. Through feature distillation, we align scoring network features with the PICG-guided image feature, enabling the scoring network to effectively incorporate the PICG information. We develop our model on a public dataset and evaluate it in a real-world challenging in-house dataset. Experimental results demonstrate that our approach improves the performance of current scoring networks.

**Keywords:** PI-RADS Clinical Guidelines · Multi-modal Large Language Model · PI-RADS scoring.

---

\* These authors contributed equally.  
\*\* Corresponding author.

## 1 Introduction

Prostate Imaging Reporting and Data System (PI-RADS) plays a crucial role in diagnosing clinically significant prostate cancer on MRI images. Officially, PI-RADS scores are defined by expert-summarized morphological descriptions, namely PI-RADS Clinical Guidelines **PICG**<sup>6</sup>. These scores range from 1 to 5 across different modalities, with higher scores indicating a higher likelihood of cancer [1,19,21]. Previous PI-RADS scoring methods [23,11,8,9] use classification models, which are supervised by manual labels on discrete numbers. The annotators provide the labels by referring to relevant PICG, however, the classification model in itself does not have access to the textual guidelines when modeling the classifier. This may cause the network to miss crucial information from PICG, limiting the model’s generalizability, especially in complex tasks with limited data, varying image quality, and intricate scoring boundaries [15].

People have considered designing rule-based models to incorporate clinical guidelines into a multi-modal learning framework of images and text [13,15,27]. However, these methods often require modifications to the network architecture or necessitate additional labels. Feature distillation may offer a new perspective for addressing the current dilemma. We can employ a guideline network to integrate information from guidelines and images, followed by feature distillation to align the feature distribution of the target network with that of the guideline network. This approach avoids increasing the parameters of the target network and eliminates the need for extra data. Therefore, an efficient network (guideline network) capable of integrating image and text inputs is essential.

Multi-modal Large Language Models (MLLM) offer a straightforward example of text and image integration [6,14,2,26]. Most MLLMs are built upon large language models and incorporate modules for interacting with images in tasks such as VQA [3] and image captioning [12]. These models often utilize attention mechanisms to facilitate interactions between images and textual information [2], or directly map images into the text domain [16][20]. These models, with a large number of parameters, may not be effectively fine-tuned on small medical image datasets. LLaMA-Adapter [29] is a parameter-efficient instruction-following model, which enhances LLaMA [25] by incorporating learnable adaptation prompts as prefixes in its transformer layer. During training, only the adaptation prompt parameters are fine-tuned while the LLaMA parameters remain frozen, allowing instructions to be effectively integrated into the model. LLaMA-Adapter V2 [7], an advancement of the LLaMA-Adapter, improves visual knowledge integration by employing an early fusion strategy to insert visual tokens into LLaMA’s early transformer layer. Moreover, additional learnable parameters in LLaMA (e.g., norm, bias, and scale) are unlocked to optimize instruction integration within the model. Despite its impressive performance in computer vision tasks, LLaMA-Adapter V2 has not demonstrated its effectiveness in addressing medical tasks, especially 3D MRI volumes.

<sup>6</sup> <https://radiopaedia.org/articles/prostate-imaging-reporting-and-data-system-pi-rads-1?lang=us>

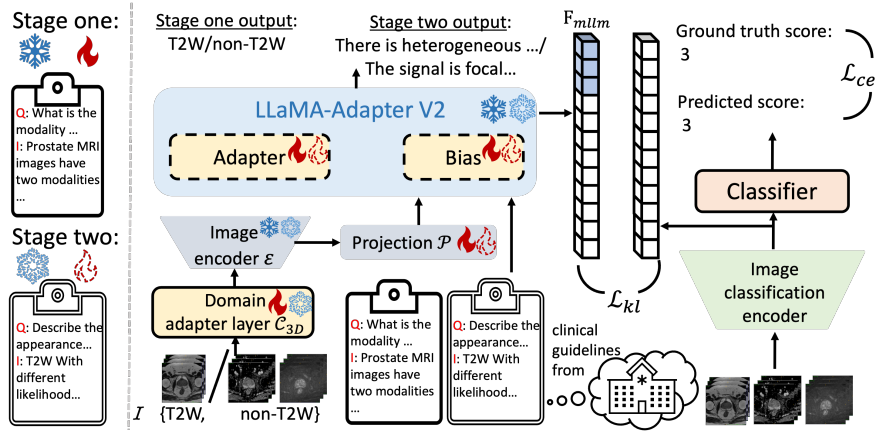


Fig. 1: Illustration of our approach.

We propose an approach for incorporating PICG into the scoring network through MLLM without increasing the parameters of the scoring network or requiring additional training data. We design a two-stage fine-tuning process to adapt MLLM to 3D MRI domain and capture PICG information. Leveraging feature distillation, we align the scoring features with the PICG-guided image features extracted from the MLLM, incorporating PICG to enhance scoring performance. In the first stage, we design a domain adapter layer to facilitate the model’s support for 3D MRI input and then adjust the instructions for MLLM to aid in distinguishing MRI modalities. These instructions offer detailed descriptions for different modalities. In the second stage, we transform PICG into instructions for the MLLM. We guide the model to generate PICG-guided image features. Due to the awareness of the multi-modal of MRI during the first stage, the instructions are structured similarly to PICG, delineating different modalities. We utilize a public dataset [18,24] for model development to ensure reproducibility. Code will be publicly available upon the acceptance. We replace each PI-RADS label with a description of the lesion corresponding to PICG for two-stage fine-tuning. Furthermore, we compile an internal dataset from real-world clinical practices to evaluate the clinical effectiveness of our methodology. Both public and private datasets contain images of three MRI modalities, along with expert-labeled PI-RADS annotations. Experimental results indicate that our approach effectively enhances scoring performance.

## 2 Method

An overview of our proposed approach is shown in Fig 1. We first present the two-stage fine-tuning process. In stage one, we establish the domain adapter layer and adjust the instructions to adapt MLLM to the MRI domain. Subsequently,

we elaborate on the instruction employed to direct MLLM in producing PICG-guided image features. Lastly, we demonstrate the feature distillation process from the MLLM to the scoring network.

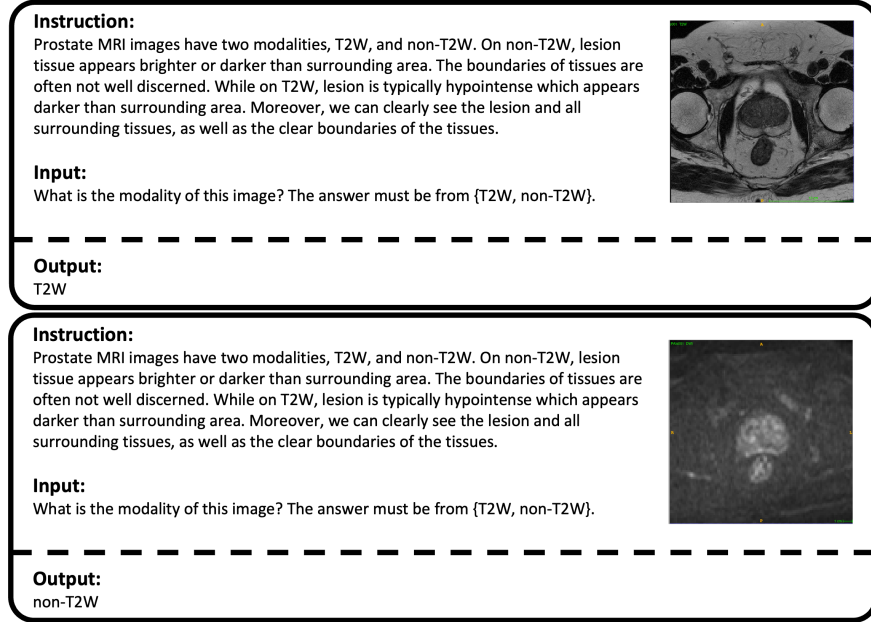


Fig. 2: Instruction of Adapting MLLM to Prostate MRI domain.

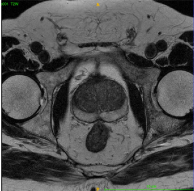
## 2.1 Stage One: Adapting MLLM to Prostate MRI Domain

**Domain Adapter Layer** LLaMA-Adapter V2 employs a vision transformer as the image encoder. Our 3D volume includes an extra “depth” dimension compared to the 2D images on which LLaMA-Adapter V2 is trained. To address this, we adapt the patch embedding layer of the transformer to a 3D convolutional layer with a kernel size of 14, which we refer to as the domain adapter layer. We denote it as  $\mathcal{C}_{3D}$ . Following I3D [5], we duplicate the pre-trained weights from the original embedding layer across the “depth” dimension to maintain the original patch division for each slice within the volume. As part of the pre-processing, the input volumes are reshaped to ensure the number of patches remains consistent with the original LLaMA-Adapter V2. Given the input 3D MRI image  $I$ , the visual prompts  $P$  are encoded as follows:

$$P = \mathcal{P}(\mathcal{E}(\mathcal{C}_{3D}(I))) \quad (1)$$

where  $\mathcal{E}$  is the rest blocks of the image encoder and  $\mathcal{P}$  refers to the multi-modal projection layer.  $P$  is added into some learnable adapter tokens, which are further fused with the text tokens embedded in the given instruction.

**Instruction:**  
 "T2W":  
 With different likelihood of clinically significant cancer, prostate MRI images can have different appearances.  
 When the likelihood is very low, there will be normal appearing transition zone (rare) or a round, completely encapsulated nodule (typical nodule of benign prostatic hyperplasia).  
 When the likelihood is low, there will be a mostly encapsulated nodule or a homogeneous circumscribed nodule without encapsulation (atypical nodule), or a homogeneous mildly hypointense area between nodules in the image.  
 When the likelihood is intermediate, there is heterogeneous signal intensity with obscured margins.  
 When the likelihood is high, there will be lenticular or non-circumscribed, homogeneous, moderately hypointense, which is less than 1.5 cm in greatest dimension in the image.  
 When the likelihood is very high, there will be a lenticular or non-circumscribed, homogeneous, moderately hypointense, which is larger than 1.5 cm in greatest dimension or definite extraprostatic extension/invasive behavior.




**Input:**  
 Describe the appearance of this MRI image.

---

**Output:**  
 There is heterogeneous signal intensity with obscured margins in the images.

**Instruction:**  
 "non-T2W":  
 "With different likelihood of clinically significant cancer, prostate MRI images can have different appearances. Signal intensity in the lesion is visually compared to the average signal of normal prostate tissue elsewhere in the same histologic zone. If normal prostate tissue signal is low, then the lesion signal is high. If normal prostate tissue signal is high, then the lesion signal is low. The lesion signal is called an abnormal signal.  
 If the cancer likelihood is very low, the signal will be normal.  
 If the likelihood is low, there will be linear/wedge shaped abnormal signal.  
 If the likelihood is intermediate, there will be focal (discrete and different from background), mild/moderate abnormal signal  
 If the likelihood is high, there will be focal, marked abnormal signal, which is less than 1.5 cm in greatest dimension  
 If the likelihood is very high, there will be focal, marked abnormal signal, which is larger than 1.5 cm in greatest dimension or definite extraprostatic extension/invasive behavior."



**Input:**  
 Describe the appearance of this MRI image.

---

**Output:**  
 There is heterogeneous signal intensity with obscured margins in the images.

Fig. 3: Instruction of Generating PICG-guided Image Features.

**Instruction Design and Fine-tuning Details** We fine-tune the LLaMA-Adapter V2 model to distinguish “T2W” and “non-T2W” (ADC and DWI) images. The instruction is shown in Fig 2 based on [7]. Following the fusion process of LLaMA-Adapter V2, we focus on fine-tuning the patch embedding layer, the multi-modal projection layer, and the bias in the LLaMA model, while keeping all other trainable parameters frozen. This approach enables fine-tuning on a single GPU. Throughout training, the model is optimized using the cross-entropy loss function.

## 2.2 Stage Two: Generating PICG-guided Image Features

**Network Settings** We maintain the existing model architecture and fine-tune the weights from the final stage. During this stage, we freeze the domain adapter layer while allowing the multi-modal projection layer and the bias in the LLaMA model to remain trainable.

**Instruction Design and Fine-tuning Details** We modify the instruction of LLaMA-Adapter V2 model to understand PICG. Our instruction of stage two is described in Fig. 3. We formulate the task to stimulate the LLaMA-Adapter V2 model to describe the lesion in the MRI image based on the PICG. This helps us obtain an instruction-incorporated representation of the MRI image. Specifically, at the end of this stage, we utilize the fine-tuned LLaMA-Adapter V2 model to generate PICG-guided features (given Fig. 3) of each sample in the training set. We take the average of token features from the last transformer layer of the model to obtain PICG-guided image features. The feature, i.e., a representation of the MRI images that incorporates the PICG, will be leveraged to guide our PI-RADS scoring task.

### 2.3 Incorporating PICG in PI-RADS Scoring by Feature Distillation

We incorporate the encoded PICG into the task using feature distillation. Specifically, we utilize the PICG-guided image feature to distill the features of the last layer of the scoring network. Denoting  $\mathbf{x}$  the output of the last feature layers of the scoring network, the Kullback-Leibler (KL) divergence loss function is used to distill the feature information as follows:

$$\mathcal{L}_{kl} = - \sum_{i=1}^N \mathbf{F}_{mllm} \log f_k(\mathbf{x}), \quad (2)$$

where  $\mathbf{F}_{mllm}$  is the PICG-guided image feature from LLaMA-Adapter V2,  $f_k$  is one fully connected layer only used in the loss function. We use  $f_k$  to align the feature size of the scoring network with that of the PICG-guided image feature. This layer will be discarded during inference.

### 2.4 Learning Process

In the first fine-tuning stage, we configure the epoch to 20, warmup epoch to 2, weight decay to 0.02, and learning rate to 0.02. In the second stage, we initialize the weights from the first stage, adjust the epoch to 60, and the warmup epoch to 5.

The overall objective function of the scoring network is as:  $\mathcal{L}_{all} = \mathcal{L}_{ce} + \alpha * \mathcal{L}_{kl}$ . where  $\mathcal{L}_{ce}$  is the cross-entropy loss. We use three representative PI-RADS scoring networks and incorporate the PICG into these networks. We leverage pre-training weights from the Kinetics-700 [4] and Moments in Times datasets [17], set the batch size to 16, employ focal loss as the loss function with weights specified as [2, 2, 1, 1, 1], and  $\gamma$  set to 2. Our optimization strategy involves using Adam with a learning rate of 5e-5 over 200 epochs. All models are trained on a single NVIDIA A40 card.

### 3 Experiments

#### 3.1 Datasets

We employed a publicly available dataset [18] for model development, which keeps our model reproducible. To assess our model, we gathered an in-house dataset derived from authentic clinical procedures, offering insights into real-world clinical applicability. Following [22,28], we note that training on the clean public dataset and validating on the real clinical dataset brings additional challenges to the model performance.

**Public Dataset for Model Development** We used the Prostate-MRI-US-Biopsy dataset [18], which comprises preoperative MRI images, along with location details and PI-RADS scores annotation of each lesion. Only MRIs with all three modalities (T2W, ADC, DWI) were incorporated resulting in a dataset of 762 lesions from 615 subjects. Consistent with [28], we isolated the regions of interest based on the location annotations and reserved 10% of the data for validation purposes.

**Private Test Set for Evaluation** We gathered T2W, ADC, and DWI images from a cohort of 206 patients. Two experienced radiologists independently evaluated these images, annotating each lesion with its respective location and PI-RADS score. Overall, our dataset comprises 206 patients and 293 lesions. Similar to the training set, we identified and extracted the lesions from the images for further analysis.

#### 3.2 Comparison with State-of-the-Art Methods

To demonstrate the effectiveness of our method, we compared it with the state-of-the-art PI-RADS scoring networks [22,10,11], as presented in Table 1. In this comparison, we did not contrast our methods with those incorporating PICG due to the need for extra labeling. All results were assessed using Accuracy, Mean Squared Error (MSE), Mean Absolute Error (MAE), Precision, Recall, and F1 metrics. Precision, Recall, and F1 scores were averaged across all classes. Our method was applied to these three scoring networks for comparison. Following the application of our method, all three scoring networks and VGG network show improvements across all metrics. Particularly, our method brings an improvement of 6.4% in accuracy and 2.9% in precision to [11]. This highlights the effectiveness of integrating PICG into scoring networks for enhancing accuracy. Additionally, our method leads to a decrease in false positives. Furthermore, the incorporation of PICG resulted in reduced MSE and MAE values across all three networks, indicating that the generated scores are closer to the ground truth. It is important to note that our proposed approach is compatible with any scoring network.

Model	Accuracy % $\uparrow$	MSE $\downarrow$	MAE $\downarrow$	Precision% $\uparrow$	Recall% $\uparrow$	F1% $\uparrow$
VGG	31.6 $\pm$ 1.4	1.38 $\pm$ 0.2	0.92 $\pm$ 0.5	17.4 $\pm$ 1.5	22.6 $\pm$ 0.8	17.4 $\pm$ 1.8
VGG+PICG	38.6 $\pm$ 2.1(+7.0)	1.09 $\pm$ 0.1	0.77 $\pm$ 0.0	21.1 $\pm$ 0.3	22.9 $\pm$ 1.2	21.0 $\pm$ 0.6
Kang et al., [11]	30.0 $\pm$ 4.0	1.43 $\pm$ 0.3	0.93 $\pm$ 0.1	13.2 $\pm$ 2.6	20.1 $\pm$ 2.5	14.5 $\pm$ 2.0
Kang et al., [11]+PICG	36.4 $\pm$ 1.0 (+6.4)	1.25 $\pm$ 0.0	0.83 $\pm$ 0.0	16.1 $\pm$ 3.6	20.9 $\pm$ 1.8	15.9 $\pm$ 2.3
Sanford et al., [22]	30.4 $\pm$ 0.4	1.61 $\pm$ 0.2	0.97 $\pm$ 0.1	17.7 $\pm$ 1.3	22.1 $\pm$ 1.7	16.1 $\pm$ 1.1
Sanford et al., [22]+PICG	35.7 $\pm$ 0.9(+5.3)	1.38 $\pm$ 0.2	0.87 $\pm$ 0.1	18.4 $\pm$ 1.2	22.0 $\pm$ 0.5	17.4 $\pm$ 1.5
Yu et al., [28]	33.8 $\pm$ 0.6	1.22 $\pm$ 0.2	0.83 $\pm$ 0.1	18.2 $\pm$ 6.1	21.8 $\pm$ 2.3	13.4 $\pm$ 3.1
Yu et al., [28]+PICG	<b>38.6</b> $\pm$ 0.4(+4.8)	1.17 $\pm$ 0.1	0.79 $\pm$ 0.0	20.4 $\pm$ 0.6	23.8 $\pm$ 1.4	20.6 $\pm$ 0.8

Table 1: Scoring performance comparison on private dataset (External test). Results are reported with the average and standard deviation over three independent runs.

loss weight $\alpha = 0.2$			loss weight $\alpha = 0.4$			loss weight $\alpha = 0.6$		
Acc.% $\uparrow$	MSE $\downarrow$	MAE $\downarrow$	Acc.% $\uparrow$	MSE $\downarrow$	MAE $\downarrow$	Acc.% $\uparrow$	MSE $\downarrow$	MAE $\downarrow$
36.2	1.24	0.83	38.6	1.26	0.82	32.4	1.70	0.99

Table 2: Different loss function weight  $\alpha$

### 3.3 Ablation Study

**Determining Loss Function Weight  $\alpha$**  Large models have strong generalization capabilities, while small models excel at specific tasks, so we need to balance the proportion of loss weights. We illustrated the experiment process of determining the optimal loss weight  $\alpha$  in Eq. 2 as shown in Table 2. We assigned three loss weights 0.2, 0.4, and 0.6, respectively. It is considerable that when the weight is set to 0.4, the model exhibits improved performance compared to when the weight is set to 0.2. However, increasing the weight to 0.6 results in a notable decrease in the model’s accuracy.

**The Effect of Two-stage Fine-tuning** We analyzed the impact of fine-tuning Multi-modal Large Language Models (MLLM) on the scoring network’s performance. We designed a comparative experiment named “baseline MLLM”. We keep the MLLM in its initialized state without fine-tuning it. Subsequently, we input the same input and instructions as pre-train into the baseline MLLM, extract features from the same positions, and conduct feature distillation. As shown in Table 3, utilizing features from the initialized MLLM resulted in a decrease in accuracy compared to using pre-trained features. Furthermore, the model’s accuracy was even lower than the results reported by Sanford et al., [22]. Similarly, following the findings of Yu et al., [28] and kang et al., [11], employing features without pre-training also led to a reduction in the model’s accuracy.

## 4 Conclusion

We introduce an innovative method that incorporates PICG into the PI-RADS scoring process using Multimodal Large Language Models (MLLM). We develop



model	w/o PICG	with PICG	baseline MLLM
Kang et al., [11]	33.8%	37.5%	33.1%
Sanford et al., [22]	30.7%	36.5%	29.7%
Yu et al., [28]	34.5%	38.9%	35.8%

Table 3: The effect of two-stage fine-tuning (We use accuracy metric and select the best performance over three independent runs.)

a two-stage fine-tuning procedure to adapt MLLM to MRI domain and understand PICG. We design a domain adapter layer to facilitate adaptation and adjust the instructions for fine-tuning. Feature distillation is employed to integrate PICG into the scoring network. Our approach boosts the performance of current scoring techniques, showcasing clinical applicability.

## References

1. Ahmed, H.U., Bosaily, A.E.S., Brown, L.C., Gabe, R., Kaplan, R., Parmar, M.K., Collaco-Moraes, Y., Ward, K., Hindley, R.G., Freeman, A., et al.: Diagnostic accuracy of multi-parametric mri and trus biopsy in prostate cancer (promis): a paired validating confirmatory study. *The Lancet* **389**(10071), 815–822 (2017)
2. Alayrac, J.B., Donahue, J., Luc, P., Miech, A., Barr, I., Hasson, Y., Lenc, K., Mensch, A., Millican, K., Reynolds, M., et al.: Flamingo: a visual language model for few-shot learning. *Advances in Neural Information Processing Systems* **35**, 23716–23736 (2022)
3. Antol, S., Agrawal, A., Lu, J., Mitchell, M., Batra, D., Zitnick, C.L., Parikh, D.: Vqa: Visual question answering. In: *Proceedings of the IEEE international conference on computer vision*. pp. 2425–2433 (2015)
4. Carreira, J., Noland, E., Hillier, C., Zisserman, A.: A short note on the kinetics-700 human action dataset. *arXiv preprint arXiv:1907.06987* (2019)
5. Carreira, J., Zisserman, A.: Quo vadis, action recognition? a new model and the kinetics dataset. In: *proceedings of the IEEE Conference on Computer Vision and Pattern Recognition*. pp. 6299–6308 (2017)
6. Dai, W., Li, J., Li, D., Tiong, A., Zhao, J., Wang, W., Li, B., Fung, P., Hoi, S.: InstructBLIP: Towards general-purpose vision-language models with instruction tuning. In: *Thirty-seventh Conference on Neural Information Processing Systems* (2023), <https://openreview.net/forum?id=vvoWPYqZJA>
7. Gao, P., Han, J., Zhang, R., Lin, Z., Geng, S., Zhou, A., Zhang, W., Lu, P., He, C., Yue, X., et al.: Llama-adapter v2: Parameter-efficient visual instruction model. *arXiv preprint arXiv:2304.15010* (2023)
8. Gravina, M., Spirito, L., Celentano, G., Capece, M., Creta, M., Califano, G., Collà Ruvolo, C., Morra, S., Imbriaco, M., Di Bello, F., et al.: Machine learning and clinical-radiological characteristics for the classification of prostate cancer in pi-rads 3 lesions. *Diagnostics* **12**(7), 1565 (2022)
9. Gu, W.j., Liu, Z., Yang, Y.j., Zhang, X.z., Chen, L.y., Wan, F.n., Liu, X.h., Chen, Z.z., Kong, Y.y., Dai, B.: A deep learning model, nafnet, predicts adverse pathology and recurrence in prostate cancer using mris. *NPJ Precision Oncology* **7**(1), 134 (2023)

10. Jiang, W., Lin, Y., Vardhanabhuti, V., Ming, Y., Cao, P.: Joint cancer segmentation and pi-rads classification on multiparametric mri using minisegcaps network. *Diagnostics* **13**(4), 615 (2023)
11. Kang, Z., Xiao, E., Li, Z., Wang, L.: Deep learning based on resnet-18 for classification of prostate imaging-reporting and data system category 3 lesions. *Academic Radiology* (2024)
12. Karpathy, A., Fei-Fei, L.: Deep visual-semantic alignments for generating image descriptions. In: *Proceedings of the IEEE conference on computer vision and pattern recognition*. pp. 3128–3137 (2015)
13. Koh, P.W., Nguyen, T., Tang, Y.S., Mussmann, S., Pierson, E., Kim, B., Liang, P.: Concept bottleneck models. In: *International conference on machine learning*. pp. 5338–5348. PMLR (2020)
14. Li, C., Wong, C., Zhang, S., Usuyama, N., Liu, H., Yang, J., Naumann, T., Poon, H., Gao, J.: Llava-med: Training a large language-and-vision assistant for biomedicine in one day. *Advances in Neural Information Processing Systems* **36** (2024)
15. Lin, M., Feragen, A., Bashir, Z., Tolsgaard, M.G., Christensen, A.N.: I saw, i conceived, i concluded: Progressive concepts as bottlenecks. *arXiv preprint arXiv:2211.10630* (2022)
16. Liu, H., Li, C., Wu, Q., Lee, Y.J.: Visual instruction tuning. *Advances in neural information processing systems* **36** (2024)
17. Monfort, M., Andonian, A., Zhou, B., Ramakrishnan, K., Bargal, S.A., Yan, T., Brown, L., Fan, Q., Gutfreund, D., Vondrick, C., et al.: Moments in time dataset: one million videos for event understanding. *IEEE transactions on pattern analysis and machine intelligence* **42**(2), 502–508 (2019)
18. Natarajan, S., Priester, A., Margolis, D., Huang, J., Marks, L.: Prostate mri and ultrasound with pathology and coordinates of tracked biopsy (prostate-mri-us-biopsy). *Cancer Imaging Arch* **10**, 7937 (2020)
19. Park, S.Y., Jung, D.C., Oh, Y.T., Cho, N.H., Choi, Y.D., Rha, K.H., Hong, S.J., Han, K.: Prostate cancer: Pi-rads version 2 helps preoperatively predict clinically significant cancers. *Radiology* **280**(1), 108–116 (2016)
20. Peng, B., Li, C., He, P., Galley, M., Gao, J.: Instruction tuning with gpt-4. *arXiv preprint arXiv:2304.03277* (2023)
21. Purysko, A.S., Baroni, R.H., Giganti, F., Costa, D., Renard-Penna, R., Kim, C.K., Raman, S.S.: Pi-rads version 2.1: a critical review, from the ajr special series on radiology reporting and data systems. *American Journal of Roentgenology* **216**(1), 20–32 (2021)
22. Sanford, T., Harmon, S.A., Turkbey, E.B., Kesani, D., Tuncer, S., Madariaga, M., Yang, C., Sackett, J., Mehralivand, S., Yan, P., et al.: Deep-learning-based artificial intelligence for pi-rads classification to assist multiparametric prostate mri interpretation: A development study. *Journal of Magnetic Resonance Imaging* **52**(5), 1499–1507 (2020)
23. Schelb, P., Kohl, S., Radtke, J.P., Wiesenfarth, M., Kickingeder, P., Bickelhaupt, S., Kuder, T.A., Stenzinger, A., Hohenfellner, M., Schlemmer, H.P., et al.: Classification of cancer at prostate mri: deep learning versus clinical pi-rads assessment. *Radiology* **293**(3), 607–617 (2019)
24. Sonn, G.A., Natarajan, S., Margolis, D.J., MacAiran, M., Lieu, P., Huang, J., Dorey, F.J., Marks, L.S.: Targeted biopsy in the detection of prostate cancer using an office based magnetic resonance ultrasound fusion device. *The Journal of urology* **189**(1), 86–92 (2013)

25. Touvron, H., Lavril, T., Izacard, G., Martinet, X., Lachaux, M.A., Lacroix, T., Rozière, B., Goyal, N., Hambro, E., Azhar, F., et al.: Llama: Open and efficient foundation language models. arXiv preprint arXiv:2302.13971 (2023)
26. Wu, J., Gan, W., Chen, Z., Wan, S., Philip, S.Y.: Multimodal large language models: A survey. In: 2023 IEEE International Conference on Big Data (BigData). pp. 2247–2256. IEEE (2023)
27. Yang, Y., Panagopoulou, A., Zhou, S., Jin, D., Callison-Burch, C., Yatskar, M.: Language in a bottle: Language model guided concept bottlenecks for interpretable image classification. In: Proceedings of the IEEE/CVF Conference on Computer Vision and Pattern Recognition. pp. 19187–19197 (2023)
28. Yu, R., Jiang, K.w., Bao, J., Hou, Y., Yi, Y., Wu, D., Song, Y., Hu, C.H., Yang, G., Zhang, Y.D.: Pi-radsai: introducing a new human-in-the-loop ai model for prostate cancer diagnosis based on mri. *British Journal of Cancer* **128**(6), 1019–1029 (2023)
29. Zhang, R., Han, J., Zhou, A., Hu, X., Yan, S., Lu, P., Li, H., Gao, P., Qiao, Y.: Llama-adapter: Efficient fine-tuning of language models with zero-init attention. arXiv preprint arXiv:2303.16199 (2023)